

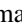
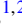






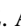







Single-particle and dipole excitations in  $^{62}\text{Co}$ 

N. Sensharma <sup>1,2,\*</sup> A. D. Ayangeakaa <sup>1,2,†</sup> R. V. F. Janssens <sup>1,2</sup> Q. B. Chen <sup>3</sup> S. Zhu <sup>4,‡</sup> M. Alcorta <sup>5,§</sup>  
 M. P. Carpenter <sup>5</sup> E. A. McCutchan <sup>4,5</sup> F. G. Kondev <sup>5</sup> T. Lauritsen <sup>5</sup> D. Seweryniak <sup>5</sup> C. R. Hoffman <sup>5</sup>  
 A. M. Rogers <sup>5,6</sup> A. Gade <sup>7,8</sup> T. Baugher <sup>7,8</sup> and P. Chowdhury <sup>6</sup>

<sup>1</sup>*Department of Physics and Astronomy, University of North Carolina Chapel Hill, North Carolina 27599, USA*

<sup>2</sup>*Triangle Universities Nuclear Laboratory, Duke University, Durham, North Carolina 27708, USA*

<sup>3</sup>*Department of Physics, East China Normal University, Shanghai 200241, China*

<sup>4</sup>*National Nuclear Data Center, Brookhaven National Laboratory, Upton, New York 11973, USA*

<sup>5</sup>*Physics Division, Argonne National Laboratory, Argonne, Illinois 60439, USA*

<sup>6</sup>*Department of Physics, University of Massachusetts, Lowell, Massachusetts 01854, USA*

<sup>7</sup>*National Superconducting Cyclotron Laboratory, Michigan State University, East Lansing, Michigan 48824, USA*

<sup>8</sup>*Department of Physics and Astronomy, Michigan State University, East Lansing, Michigan 48824, USA*



(Received 15 March 2022; accepted 5 April 2022; published 18 April 2022)

An extensive study of the level structure of  $^{62}\text{Co}$  has been performed following a complex multinucleon transfer reaction,  $^{26}\text{Mg}(^{48}\text{Ca}, 2\alpha 3npy)^{62}\text{Co}$ , at beam energies of 275, 290, and 320 MeV. The combination of the Gammasphere array, the fragment mass analyzer, and a focal-plane ionization chamber was used to identify and delineate excited levels in  $^{62}\text{Co}$ . A considerable extension to the  $^{62}\text{Co}$  level scheme is proposed with firm spin-parity values assigned on the basis of angular distribution and correlation analyses. Various level sequences built upon states of single-particle character have been observed, and an interpretation of these structures in the framework of the spherical shell model is presented. At moderate spins, two dipole bands have been observed and, based on their phenomenological study, a possible magnetic rotation character is suggested. However, theoretical calculations performed using the particle rotor model support magnetic rotation for only one of these dipole bands.

DOI: [10.1103/PhysRevC.105.044315](https://doi.org/10.1103/PhysRevC.105.044315)

## I. INTRODUCTION

The evolution of shell structure of neutron-rich nuclei in the  $A \approx 60$  region has been a subject of much interest for the past few decades. Indeed, several studies have been performed in order to achieve a consolidated and consistent understanding of the structure of these nuclei (see, for example, Refs. [1–22]). On the basis of systematic studies of the energies of the first  $2^+$  states, reduced transition probabilities and precision mass measurements, evidence for the existence of new subshell closures was observed at  $N = 40$  [1,7,23],  $N = 32$  [8–13,15], and  $N = 34$  [14–17]. Further investigation in the vicinity of these subshell closures (Refs. [3,4,18,19], for example) have shown that single-particle excitations within the underlying  $fp$  shell are a dominant feature in the low-spin region. Moreover, at higher spins, the promotion of particles into the next shell, particularly the  $g_{9/2}$  intruder orbital, was seen to give rise to considerable collectivity in the Cr and Fe isotopic chains [20–22], and this was recently also reported to be the case in  $^{61}\text{Co}$  [5] and  $^{62}\text{Cu}$  [6]. Shell evolution in this

mass region has also been investigated by Ref. [24], where the  $\beta$ -decay chain starting from  $^{66}\text{Mn}$  to  $^{66}\text{Ni}$  was studied and a progression from deformed to spherical nuclear shapes was proposed.

The studies above highlight the need to document further the intrinsic structure of neutron-rich nuclei in the  $A \approx 60$  region. Indeed, while several even-even and odd- $A$  nuclei in this region have been investigated in the recent past, only limited information is available for any of the odd-odd counterparts. This is the case, for example, for  $^{62}\text{Co}$ , where the low-spin structure is relatively unknown. With  $Z = 27$  and  $N = 35$ ,  $^{62}\text{Co}$  represents a proton hole in the  $f_{7/2}$  orbit, and lies midshell in neutron number between  $N = 32$  and 40, making it ideal to study single-particle shell-model configurations. In particular, an opportunity presents itself to test further the applicability of effective interactions that have been proposed to account for the subshell closures at  $N = 32$  and 34 reported above. Furthermore, with the presence of 22 valence nucleons (when considering a  $^{40}\text{Ca}$  core),  $^{62}\text{Co}$  also offers possibilities for enhanced collectivity at higher spins.

The earliest works on this nucleus are those reported in Refs. [25,26] where the half-lives of the ground state [ $T_{1/2} = 1.50(4)$  min] and the first excited, nearly degenerate isomeric state [with  $T_{1/2} = 13.91(5)$  min] were measured following  $^{62}\text{Co}$   $\beta$  decay. At the time, the energy separation between

\* nsensharma@unc.edu

† ayangeak@unc.edu

‡ Deceased.

§ Present address: TRIUMF, Vancouver, British Columbia V6T 4A3, Canada.

these levels was only tentatively reported. These investigations were followed by a study of the  $(d, \alpha)$  reaction on a  $^{64}\text{Ni}$  target, where spin-parities and excitation energies of the populated  $^{62}\text{Co}$  levels were presented up to approximately 2.8 MeV [27]. Based on the shape of the angular distribution curve and results of distorted wave Born approximation (DWBA) calculations, the spin of the ground state was determined to favor  $J^\pi = 1^+$  or  $2^+$ , while that of the first-excited isomeric state at 22 keV was found to be consistent with  $J^\pi = 5^+$ . The latter assignment was made in analogy to the  $^{62}\text{Ni}(d, \alpha)^{60}\text{Co}$  reaction as the angular distribution displayed the same characteristic deviation from an  $L = 4$ ,  $J^\pi = 4^+$  transition. Following the same reasoning, it was demonstrated that the  $2^+$  ground state and the  $5^+$  first excited state at 22 keV are multiplets of the dominant configuration,  $(\pi 1f_{7/2}^{-1} \otimes \nu 2p_{3/2}^1)$  [27]. Similarly, in analogy to the  $^{60}\text{Co}$  ground-state transition, the level at 611 keV was assigned a  $5^+$  spin-parity, with a configuration symmetric to that of its first excited counterpart:  $(\pi 2p_{3/2}^1 \otimes \nu 1f_{7/2}^{-1})$ .

The first observation of  $\gamma$ -ray transitions depopulating low-spin yrast levels in  $^{62}\text{Co}$  was reported in Ref. [28] following a fusion evaporation reaction induced by an  $^{18}\text{O}$  beam on a  $^{48}\text{Ca}$  target. Tentative spin and parity assignments to the levels up to  $I^\pi = 8^+$  were proposed on the basis of angular distribution measurements. In another study [29], four new low-energy  $\gamma$  transitions associated with  $^{62}\text{Co}$  recoils were identified, but not placed in the level scheme due to a lack of coincidence information. Since then, not much progress has been made in the study of  $^{62}\text{Co}$  until the present work, which aims to expand the spectroscopic data available for this odd-odd nucleus and to provide a more complete picture of the underlying level structure. In this paper, we present results on the observation of level structures in  $^{62}\text{Co}$  produced via the complex multinucleon transfer reaction  $^{26}\text{Mg}(^{48}\text{Ca}, 2\alpha 3n p \gamma)^{62}\text{Co}$ . The observed single-particle states are interpreted within the framework of the spherical shell-model using the GXPF1A effective interaction [30]. In addition, two dipole bands are also observed at moderate spins. These are compared with similar structures in neighboring nuclei, and further elucidated using particle rotor model (PRM) calculations.

## II. EXPERIMENT

The data presented in this paper are part of a larger set obtained in a complex multinucleon transfer experiment carried out at the Argonne National Laboratory. A brief description of the experimental procedure is summarized below. More detailed descriptions of the experiment are, for example, provided in Refs. [3–5]. Excited states in the odd-odd  $^{62}\text{Co}$  nucleus were populated via the  $^{26}\text{Mg}(^{48}\text{Ca}, 2\alpha 3n p \gamma)^{62}\text{Co}$  inverse-kinematic, multinucleon transfer reaction at beam energies of 275, 290, and 320 MeV. The  $^{48}\text{Ca}$  beam was provided by the Argonne tandem linear accelerator system (ATLAS) and the emitted  $\gamma$  rays were detected using the Gammasphere array [31]. This spectrometer, which comprised 101 Compton suppressed HPGe detectors at the time of the experiment, was used in conjunction with the fragment

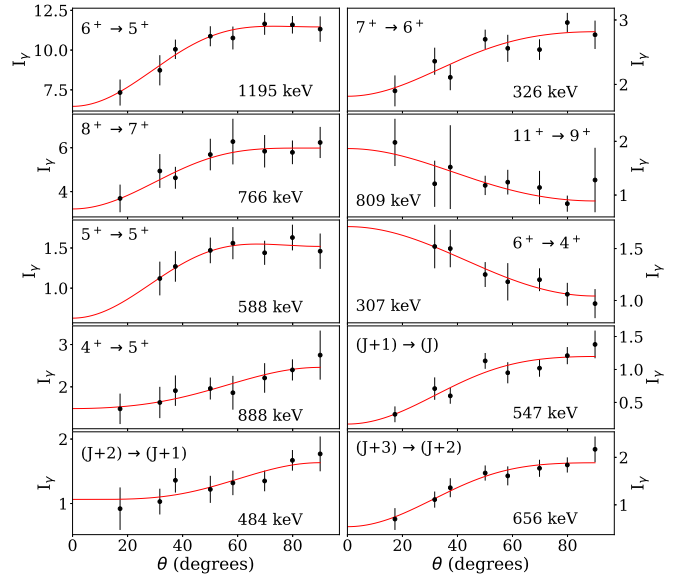


FIG. 1. Angular distributions for some of the  $\gamma$  transitions found in the level scheme of  $^{62}\text{Co}$  (see Fig. 2). Experimental data are shown as black circles while the angular distribution fit is the red curve.

mass analyzer (FMA) and a microchannel plate (MCP) detector placed at the focal plane to provide clean channel selection by dispersing the residues according to their mass-to-charge ratios ( $M/q$ ). The MCP was followed by a threefold ionization chamber, which provided  $Z$  identification. Gamma rays associated with  $^{62}\text{Co}$  residues were sorted into symmetrized  $\gamma$ - $\gamma$  coincidence matrices for subsequent analysis with the RADWARE suite of codes [32]. Energy and efficiency calibrations were performed with the standard radioactive sources— $^{152}\text{Eu}$  and  $^{56}\text{Co}$ .

Level sequences, spins, and parities for the various excited states were assigned on the basis of  $\gamma$ - $\gamma$  coincidence relationships, angular distributions, and two-dimensional angular correlation ratios. For angular distribution measurements, data from symmetric positions in Gammasphere were combined into eight rings with the average angle values,  $\theta = 17.2^\circ, 31.2^\circ, 37.2^\circ, 50.2^\circ, 58.2^\circ, 69.2^\circ, 79.2^\circ,$  and  $90.2^\circ$  with respect to the beam direction. Spectra from each ring were corrected for efficiency and the extracted intensities were fitted with the standard angular distribution function:

$$W(\theta) = 1 + A_2 P_2(\cos \theta) + A_4 P_4(\cos \theta), \quad (1)$$

where  $P_2$  and  $P_4$  are the associated Legendre polynomials. The angular distribution coefficients,  $A_2$  and  $A_4$ , were extracted using a Markov-chain Monte Carlo (MCMC) sampling technique. This technique has been described in detail in Ref. [33], and the various steps to obtain the angular distribution parameters are enumerated in Ref. [34]. In the present work, a simple convention that associates a positive  $A_2$  value with pure  $\Delta I = 2$  transitions and a negative one with mixed  $\Delta I = 1$  transitions has been adopted. Angular distribution plots for some of the transi-

TABLE I.  $\gamma$ -ray energies, relative intensities, energy of the initial state, initial and final spins, angular correlation ratios ( $R_{ac}$ ), experimental angular distribution coefficients ( $A_2$  and  $A_4$ ), and adopted multiplicities for the transitions shown in Fig. 2.

$E_\gamma$ (keV)	$I_\gamma$	$E_i$ (keV)	$I_i^\pi \rightarrow I_f^\pi$	$R_{ac}$	$A_2$	$A_4$	Multiplicity
306.8(2)	8(1)	1216.8(1)	$6^+ \rightarrow 4^+$	1.03(9)	0.35(16)	0.01(21)	$E2$
325.7(1)	58(3)	1542.6(1)	$7^+ \rightarrow 6^+$	0.83(4)	-0.24(6)	-0.05(8)	$M1 + E2$
371(1)	4(1)	3169.1(2)	$9^+ \rightarrow 8^+$	0.77(31)	-	-	$M1 + E2$
438.9(4)	1(1)	3607.9(5)	$10^+ \rightarrow 9^+$	0.72(19)	-	-	$M1 + E2$
483.4(9)	4(1)	4048.8(4)	$10^+ \rightarrow 9^+$	0.84(13)	-	-	$M1 + E2$
483.5(3)	3(1)	x+1030.5	$J + 2 \rightarrow J + 1$	0.71(7)	-0.32(13)	0.10(19)	$M1 + E2$
489.0(2)	3(1)	2797.9(3)	$8^+ \rightarrow 8^+$	0.81(57)	-	-	$M1 + E2$
547.0(3)	5(1)	x+547.0	$J + 1 \rightarrow J$	0.82(20)	-0.64(11)	-0.18(15)	$M1 + E2$
587.7(3)	9(1)	2130.2(3)	$8^+ \rightarrow 7^+$	0.89(16)	-0.37(19)	-0.05(27)	$M1 + E2$
588.4(2)	15(2)	610.6(2)	$5^+ \rightarrow 5^+$	0.83(8)	-0.34(19)	-0.21(24)	$M1 + E2$
606.2(2)	13(1)	1216.8(1)	$6^+ \rightarrow 5^+$	0.89(9)	-0.45(9)	-0.09(12)	$M1 + E2$
655.5(3)	5(1)	x+1686.0	$J + 3 \rightarrow J + 2$	0.77(22)	-0.50(10)	-0.16(13)	$M1 + E2$
674.4(4)	2(1)	4723.2(4)	$11^+ \rightarrow 10^+$	0.80(22)	-0.37(18)	-0.18(26)	$M1 + E2$
679(2)	3(1)	2960(2)	$4^+ \rightarrow 6^+$	1.31(45)	-	-	$E2$
694(6)	0.1(5)	4284(7)	$12^+ \rightarrow 10^+$	1.20(64)	-	-	$E2$
744.7(4)	3(1)	4723.2(4)	$11^+ \rightarrow 11^+$	0.77(16)	-	-	$M1 + E2$
766.4(1)	54(3)	2308.9(2)	$8^+ \rightarrow 7^+$	0.90(3)	-0.29(9)	-0.12(13)	$M1 + E2$
773(1)	1(1)	4381(1)	$11^+ \rightarrow 10^+$	0.80(17)	-	-	$M1 + E2$
794.9(4)	3(1)	x+2480.9	$J + 4 \rightarrow J + 3$	0.82(36)	-0.56(12)	-0.30(17)	$M1 + E2$
809.4(2)	11(1)	3978.5(3)	$11^+ \rightarrow 9^+$	1.20(11)	0.53(23)	0.05(25)	$E2$
813.6(9)	0.4(6)	3122.6(9)	$9^+ \rightarrow 8^+$	0.96(32)	-	-	$M1 + E2$
860.1(1)	26(2)	3169.1(2)	$9^+ \rightarrow 8^+$	0.86(5)	-0.23(13)	-0.08(20)	$M1 + E2$
880.0(4)	4(1)	4048.8(4)	$10^+ \rightarrow 9^+$	0.73(18)	-	-	$M1 + E2$
887.9(3)	15(3)	910.0(2)	$4^+ \rightarrow 5^+$	0.92(18)	-0.34(13)	0.06(17)	$M1 + E2$
888.0(2)	4(1)	x+3368.9	$J + 5 \rightarrow J + 4$	0.91(13)	-	-	$M1 + E2$
909.7(8)	1(1)	4508(2)	$11^+ \rightarrow 9^+$	1.13(19)	-	-	$E2$
1010(9)	0.1(3)	x+4378.7	$(J + 6) \rightarrow J + 5$	-	-	-	$(M1 + E2)$
1022(1)	0.3(5)	5001(1)	$12^+ \rightarrow 11^+$	0.65(30)	-	-	$M1 + E2$
1050(5)	3(3)	3331(5)	$(7^+) \rightarrow 6^+$	-	-	-	$(M1 + E2)$
1089.4(6)	2(1)	5812.6(7)	$12^+ \rightarrow 11^+$	0.90(11)	-	-	$M1 + E2$
1135.2(9)	1(1)	6948(1)	$(13^+) \rightarrow 12^+$	-	-	-	$(M1 + E2)$
1182(1)	2(1)	4304(1)	$10^+ \rightarrow 9^+$	0.71(13)	-	-	$M1 + E2$
1194.9(1)	44(5)	1216.8(1)	$6^+ \rightarrow 5^+$	0.86(4)	-0.26(5)	-0.13(7)	$M1 + E2$
1255.4(8)	1(1)	3564.8(6)	$9^+ \rightarrow 8^+$	0.74(48)	-	-	$M1 + E2$
1371(1)	3(1)	2281(1)	$6^+ \rightarrow 4^+$	1.23(63)	-	-	$E2$
1460(4)	5(1)	3590(4)	$10^+ \rightarrow 8^+$	1.37(16)	-	-	$E2$
1468(1)	2(1)	3598(1)	$9^+ \rightarrow 8^+$	0.97(21)	-	-	$M1 + E2$
1574(4)	1(1)	3704(4)	$10^+ \rightarrow 8^+$	1.24(43)	-	-	$E2$
1581(4)	1(1)	2797.9(3)	$8^+ \rightarrow 6^+$	1.36(83)	-	-	$E2$
2050(4)	3(1)	2960(2)	$4^+ \rightarrow 4^+$	-	-	-	$(M1 + E2)$
2245(3)	1(1)	3155(3)	$(5^+) \rightarrow 4^+$	-	-	-	-

tions and the adopted initial and final spins are presented in Fig. 1.

For transitions with weak intensities, a two-dimensional angular correlation ratio,  $R_{ac}$  was used. This is defined as the normalized ratio of  $\gamma$ -ray intensities observed in detectors placed at forward or backward angles to those observed in detectors placed at  $90^\circ$  with respect to the beam direction. Here, three coincidence matrices were created corresponding to  $\gamma$  rays detected at forward ( $31.2^\circ$ ,  $37.2^\circ$ ,  $50.2^\circ$ ), backward ( $129.2^\circ$ ,  $142.2^\circ$ ,  $148.2^\circ$ ,  $162.2^\circ$ ), and middle ( $69.2^\circ$ ,  $79.2^\circ$ ,  $80.2^\circ$ ,  $90.2^\circ$ ,  $99.2^\circ$ ,  $100.2^\circ$ ,  $110.2^\circ$ ) angles on one axis and  $\gamma$  rays detected at all angles grouped on the other. Placing energy gates on the all-angle axis, the intensity of coincident

$\gamma$  rays can be determined and the ratio  $R_{ac}$  calculated as [35]

$$R_{ac} = \frac{I_{\text{forward/backward}}^{\gamma_2}(\text{Gate}_{\text{all } \theta}^{\gamma_1})}{I_{\text{middle}}^{\gamma_2}(\text{Gate}_{\text{all } \theta}^{\gamma_1})}, \quad (2)$$

where  $\gamma_1$  and  $\gamma_2$  are two successive  $\gamma$  transitions and  $\theta$  is the angle with respect to the direction of the beam. Similar to angular distributions,  $R_{ac}$  can be used to distinguish between  $\Delta I = 1$  and  $\Delta I = 2$  transitions. In the present analysis, a stretched quadrupole transition ( $\Delta I = 2$ ) is characterized by an  $R_{ac}$  value greater than 1.0 while a value of  $R_{ac} < 0.8$  indicates a dipole  $\Delta I = 1$  transition [5]. The  $A_2$  and  $A_4$  coefficients, the extracted  $R_{ac}$  ratios, and the adopted multiplicities

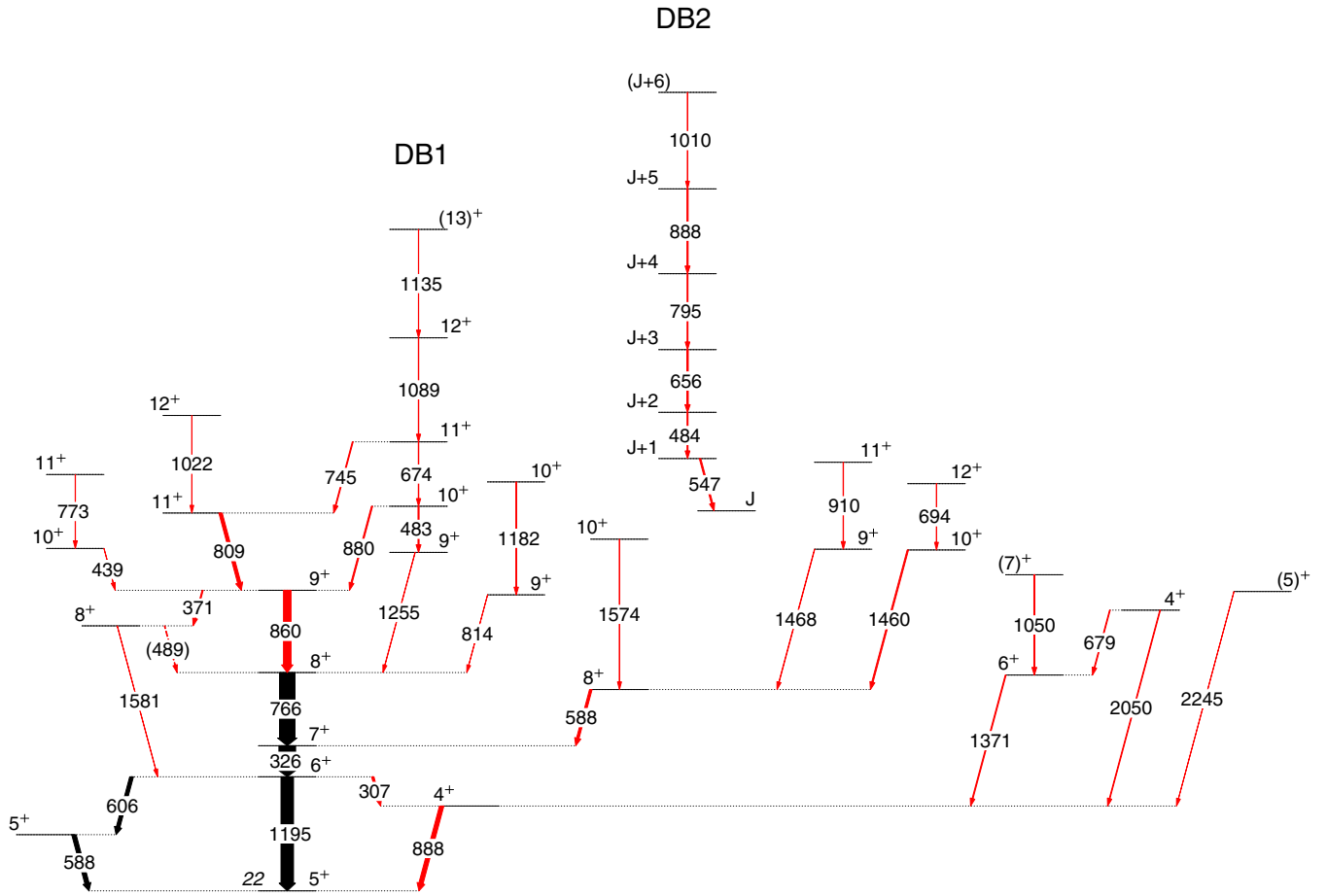


FIG. 2. Level scheme of  $^{62}\text{Co}$  developed in the present work. Note that the lowest level shown is a  $5^+$  isomeric level with  $E_x = 22$  keV. The newly added transitions are given in red with the tentative placements shown in brackets.

for transitions observed in the present study are listed in Table I, together with information on transition energies and intensities as well as on placements in the level scheme.

### III. LEVEL SCHEME

The complete decay scheme of  $^{62}\text{Co}$  established in the present work is displayed in Fig. 2. This scheme was developed using a combination of energy sums, intensity balances, and  $\gamma$ - $\gamma$  coincidence relationships. While the low-spin part is similar to that presented in Refs. [27–29,36], the current scheme presents a significant extension with excitations up to 6.9 MeV and firm assignments of spins and parities. Figure 3 provides the background-subtracted and efficiency-corrected total projection spectrum obtained in coincidence with  $^{62}\text{Co}$  recoils. This figure highlights the dominant transitions at low spins with the 326-keV  $\gamma$  ray appearing as the most intense. Also visible is the 483 (484)-keV transition that populates the band head of the newly established dipole band, identified as DB1 (DB2), in Fig. 2. The structure and nature of these bands is discussed in detail in the next section. As noted above, the present scheme is built atop the  $5^+_1$  isomeric level located 22 keV above the ground state. The spin and parity of this  $5^+_1$  state and of the four levels depopulated by the black-colored transitions in Fig. 2 were previously established

in Refs. [27–29]. These assignments have been confirmed in the present work.

Figures 4(a) and 4(b) present spectra resulting from coincidence gates on the 1195- and 326-keV transitions, respectively. Based on the coincidence relationships and intensities observed in these gated spectra, the 1195–326–766–860-keV cascade has been established (see Fig. 2). Following a similar procedure, a few of the other low-lying  $\gamma$  rays (such as the 888-, 588-, 606-, and 307-keV transitions) have also been placed. It is important to note here that the present work is in agreement with Ref. [29] regarding

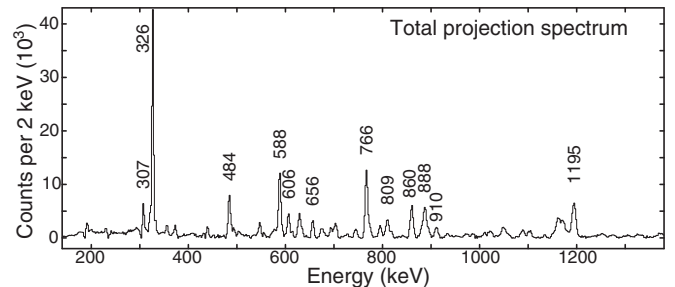


FIG. 3. Total background-corrected projection spectrum obtained from the  $^{62}\text{Co}$  coincidence matrix.

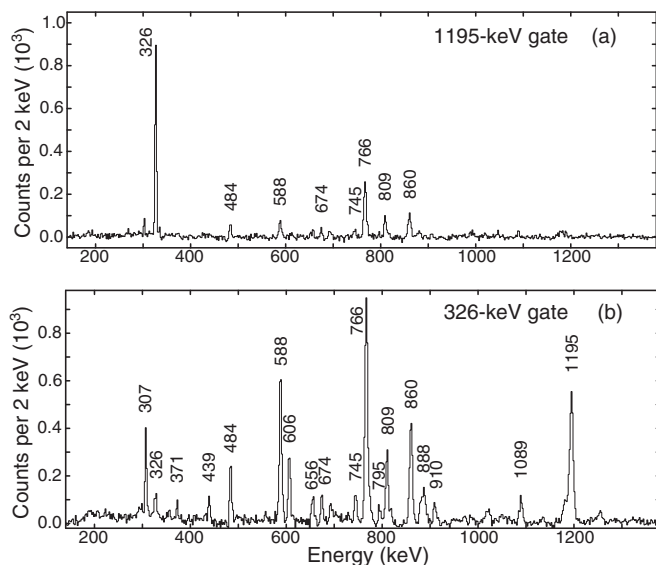


FIG. 4. The observed coincidence spectra resulting from a single coincidence gate on (a)  $E_\gamma = 1195$  keV and (b)  $E_\gamma = 326$  keV. The coincident  $\gamma$ -ray energies are marked against the respective energy peaks.

the placement of the 588- and 606-keV transitions linking the  $6_1^+ \rightarrow 5_2^+ \rightarrow 5_1^+$  cascade. Based on intensities and the presence of a weak 588-keV peak in the spectrum obtained by gating on the 1195-keV transition [see Fig. 4(a)], the 588-keV transition has been deduced to be a doublet, the second component of which was found to de-excite the  $8^+$  level at 2.1 MeV, and is part of the 910–1468–588-keV cascade populating the yrast  $7_1^+$  level. It is, however, observed (from Fig. 5) that the intensity of 588-keV  $\gamma$  ray depopulating the  $5_2^+$  level is approximately twice that of the preceding 606-keV transition. With the 326–606–588-keV cascade, the same intensities would be expected for the 588- and 606-keV transitions in a coincidence spectrum gated with the 766-keV  $\gamma$  ray. This excess intensity of the 588-keV  $\gamma$  ray has, therefore, been attributed to the possible presence of another structure feeding into the  $5_2^+$  state that would de-excite via the 588-keV transition to the  $5_1^+$  level. Evidence of this structure has not been observed in the present study, presumably be-

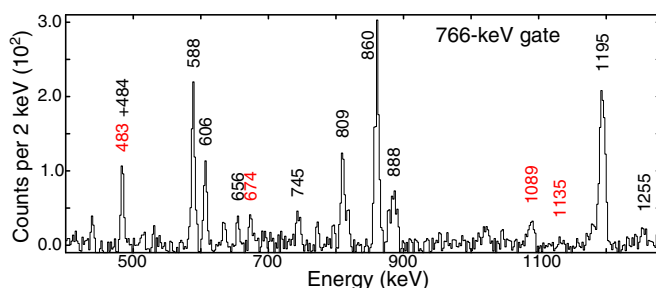


FIG. 5. The observed coincidence spectrum resulting from a single coincidence gate on  $E_\gamma = 766$  keV. The coincident  $\gamma$ -ray energies are marked against the respective energy peaks. The peaks marked in red correspond to the DB1 in-band transitions.

cause of the expected intensity being distributed over several weak transitions. It is also worth mentioning the presence of the newly established  $4_1^+$  state at 910 keV. Despite its low energy, this level was not seen in any of the previous investigations (Refs. [27,28], for example). Although the most recent study by Recchia *et al.* [29] identified two new  $\gamma$  rays (307 and 888 keV) in addition to the five lowest transitions (326, 588, 606, 766, and 1195 keV), no indication of their placement in the level scheme was provided. These two transitions have now been placed as populating (307 keV) and depopulating (888 keV) the 910-keV level, based on the lack of coincidence with the 1195-keV transition. Angular distribution and correlation analyses have identified the 307-keV transition as being of quadrupole character, and the 888-keV one as a dipole, hence a  $4^+$  spin assignment. The relevant angular distribution plots are displayed in Fig. 1.

In addition to several new levels, two rotational-like sequences, identified as DB1 and DB2 in Fig. 2, have been observed in coincidence with the low-lying structure. Band DB1, comprising the 483-, 674-, 1089-, and 1135-keV in-band transitions, is built on top of the  $I^\pi = 9^+$  band head at an excitation energy of 3.6 MeV. It feeds into the yrast structure via the 880- and 1255-keV transitions. A coincidence spectrum obtained by gating on the 766-keV  $\gamma$  ray is presented in Fig. 5 where the peaks marked in red correspond to the DB1 in-band transitions. Based on the present multipolarity analysis (see Table I), the 483-, 674-, and 1089-keV transitions within this band have been identified as  $\Delta I = 1$  transitions. The highest in-band transition of 1135 keV was too weak to perform a detailed angular distribution or correlation analysis. However, due to its placement atop a sequence of dipole transitions, a  $\Delta I = 1$  character was adopted for it as well. Similarly, the 484-, 656-, 795-, 888-, and 1010-keV cascade, labeled as DB2 in Fig. 2, has been found to have a predominantly dipole character on the basis of the angular distribution and/or correlation analysis for the 484-, 656-, 795-, 888-keV transitions, and of the continuation of the band in the case of the weak 1010-keV  $\gamma$  ray. These transitions are ordered based on their relative intensities but, unlike the DB1 band, the spins and parities have not been assigned since their decay paths to the low-energy part of the level scheme could not be firmly established. Figure 6(a) provides a coincidence spectrum resulting from the sum of all possible single coincidence gates placed on the DB2 in-band transitions. Of note is the presence of the 547-keV dipole transition (marked in red) which has been observed [see Fig. 6(b)] to be in coincidence with all the DB2 in-band transitions as well as with those linking the  $8_1^+$  state at 2.1 MeV to the 1.5-MeV  $7_1^+$  level within the yrast structure, i.e., the 588-, 1574-, and 1460-keV  $\gamma$  rays. This 547-keV  $\gamma$  ray was also found to be in coincidence with the 1050–1371–888-keV cascade feeding directly into the  $5_1^+$  isomeric state. A direct comparison of Figs. 6(a) and 6(b) reveals that, while the 326-, 766-, and 1195-keV transitions show strong coincidence relationships with the DB2 in-band transitions, they exhibit weak ones with the 547-keV  $\gamma$  ray. Based on these observations and intensity balances, it is concluded that the decay of the DB2 band proceeds through at least two pathways, with one branch connected via the 547-keV transition and other intermediate

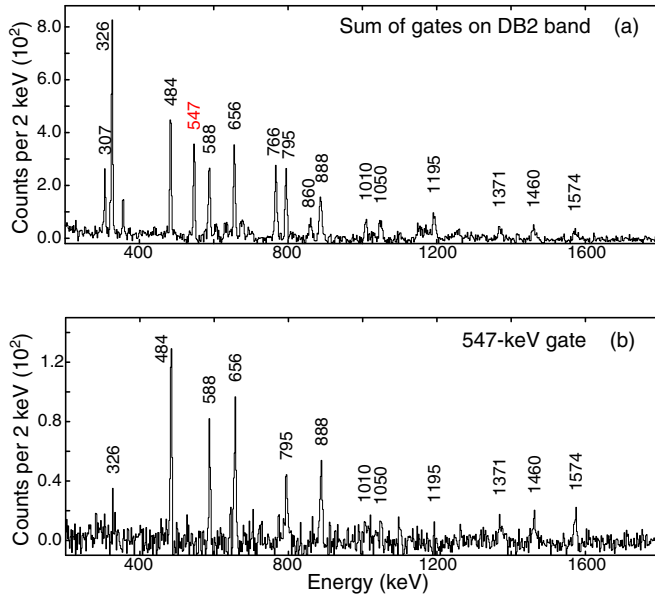


FIG. 6. The observed coincidence spectra resulting from (a) the sum of single coincidence gates on  $E_\gamma = 484, 656, 795, 888,$  and  $1010$  keV and (b) a single one on  $E_\gamma = 547$  keV. The coincident  $\gamma$ -ray energies are marked against the respective energy peaks.

transitions to the  $4^+$  state at 910 keV, and the other linking through the 766–326–1195-keV cascade in the yrast structure. These connecting transitions appeared, however, to be too weak to be observed in the coincidence spectra and, thus, no firm connection of DB2 band to the lower part of the level scheme could be established. Based on intensity and coincidence considerations, the DB2 band head energy has been deduced to be  $E_x \geq 4.5$  MeV, with a most probable spin-parity assignment being  $I^\pi \geq 10^+$ .

#### IV. DISCUSSION

To gain insight into the nature of the level structures observed in  $^{62}\text{Co}$ , large-scale shell-model calculations were performed using the NUSHELLX [37] code. These calculations were performed in the full  $fp$  model space using the GXPF1A two-body effective interaction [30]. The GXPF1A Hamiltonian is derived from a microscopic calculation based on renormalized G matrix theory with the Bonn-C interaction [38], and was recently refined by a systematic fitting of the important linear combinations of two-body matrix elements to low-lying states in the  $A = 47$ -66 nuclei [30]. Specifically, it is worth reminding that this interaction was first introduced to account for the onset of the  $N = 32$  and  $34$  subshell gaps [8,12], and highlighted the role of the monopole tensor part of the nucleon-nucleon interaction. With a  $^{40}\text{Ca}$  core, energy levels in  $^{62}\text{Co}$  were investigated as an interplay between seven valence protons and 15 valence neutrons. Figure 7 compares the shell-model calculations with the experimental level energies for the yrast states and other low-lying energy levels. While the calculations were able to correctly predict the  $2^+$  ground-state spin and parity, significant discrepancies between calculated and experimental energies are observed

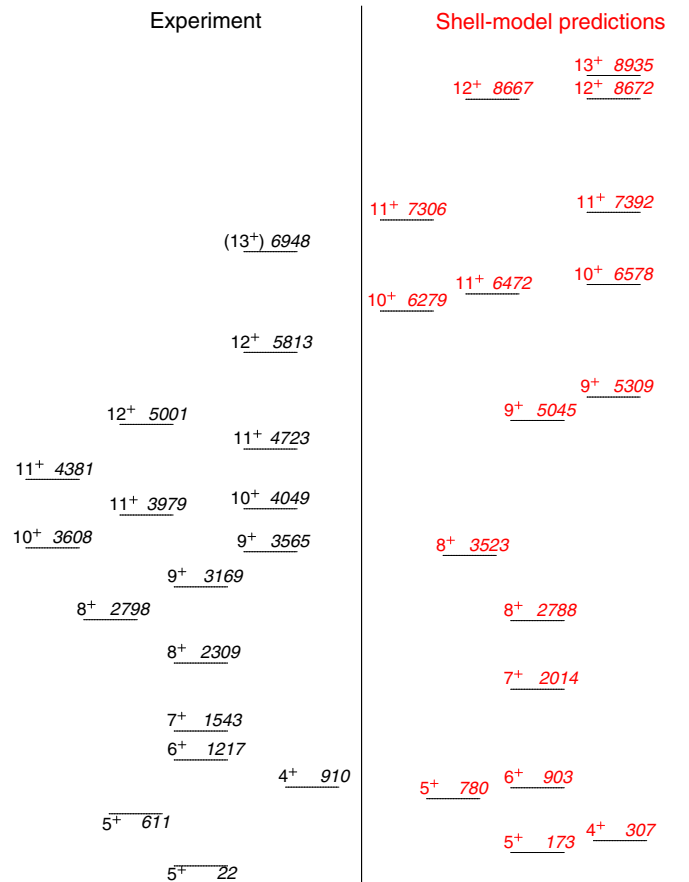


FIG. 7. Experimental level energies in  $^{62}\text{Co}$  compared with spherical shell-model calculations using the GXPF1A effective interaction. The experimental energies are given in black (left) while the shell-model predictions are in red (right).

for other levels. For instance, the first excited  $5^+$  state is calculated to be about 151 keV above the experimental value. To further quantify the comparison, a root-mean-square deviation,  $\Delta_{\text{rms}}$ , between experiment and shell-model predictions was calculated. The  $\Delta_{\text{rms}}$  is given by Ref. [39] as

$$\Delta_{\text{rms}} = \sqrt{\sum_{i=1}^N (E_{\text{exp}}^i - E_{\text{sm}}^i)^2 / N},$$

where  $E_{\text{exp}}^i$  and  $E_{\text{sm}}^i$  are the respective experimental and shell-model level energies of the  $i$ th state and  $N$  is the total number of states used in the calculation. For  $E \leq 3$  MeV, a value  $\Delta_{\text{rms}} \approx 430$  keV was obtained. This deviation was found to increase substantially for level energies beyond  $E \geq 3.5$  MeV. A high value of  $\Delta_{\text{rms}}$  indicates the failure of the chosen model space to successfully reproduce the experimental energy levels. It is worth pointing out that a deviation in  $\Delta_{\text{rms}}$  of the same magnitude was observed in the case of  $^{61}\text{Co}$  [5] for levels with  $I^\pi \geq 17/2^-$ . In the latter work, the absence of the  $g_{9/2}$  neutron orbital within the  $fp$  model space used by the GXPF1A interaction was proposed to be responsible for the observed discrepancy at high spin. Following this interpretation further in the case of  $^{62}\text{Co}$  then points to a larger role for

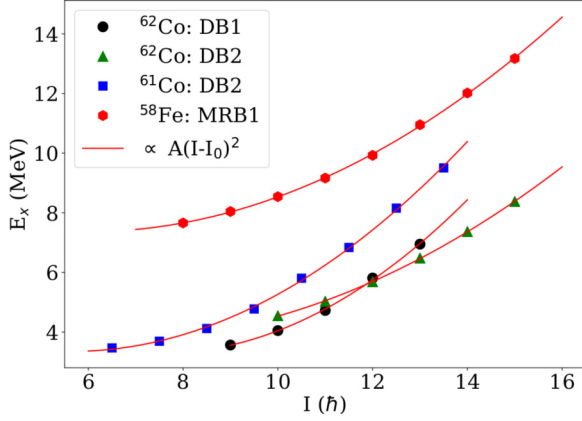


FIG. 8. Excitation energy as a function of spin for DB1 (black circles) and DB2 (green triangles) bands in  $^{62}\text{Co}$ . Also shown for comparison are the DB2 band in  $^{61}\text{Co}$  (blue squares) and the MRB1 band in  $^{58}\text{Fe}$  (red hexagons). For each of the bands, the red curve corresponds to a fit proportional to the relation  $A(I - I_0)^2$  (see text).

this  $g_{9/2}$  orbital, even in the description of lower excitations. Calculations with a larger model space are beyond the scope of the present work.

As mentioned above, two rotational-like bands have also been observed at moderate spins in addition to the low-spin structure of single-particle character. The DB1 band has been observed up to  $I^\pi = (13^+)$  with an excitation energy of 6.9 MeV, and consists of four strong  $\Delta I = 1$  in-band transitions. A connection to the low-spin structure could not be established for the DB2 band. However, just like the DB1 band, the DB2 sequence is also comprised of strong  $\Delta I = 1$  in-band transitions. No crossover  $\Delta I = 2$  transitions have been observed in either of these bands. With the observation of similar dipole bands in the nearby nuclei— $^{61}\text{Co}$  [5] and  $^{58}\text{Fe}$  [39]—where magnetic rotation was suggested, the existence of DB1 and DB2 bands in  $^{62}\text{Co}$  is, perhaps, not surprising and can potentially be considered to be of the same origin. To investigate this interpretation further, the formalism based on the shears mechanism developed in Refs. [40,41] was utilized.

Magnetic rotation was first observed in neutron-deficient Pb isotopes, where the tilted axis cranking (TAC) model was used to interpret the bands [42]. Magnetic rotation bands are seen when the total angular momentum is generated by the alignment of the proton and the neutron spins ( $\mathbf{j}_\pi$  and  $\mathbf{j}_\nu$ , respectively) in a manner reminiscent of the closing of a pair of shears. These bands are characterized by a regular sequence of strong  $M1$  transitions with little or no crossovers. For such bands, Refs. [40,41] showed that the energies of the levels involved follow the pattern:  $(E - E_0) \approx A(I - I_0)^2$ , where  $E_0$  and  $I_0$  correspond to the energy and spin of the band head, respectively. The observed relationship between the excitation energy and the angular momentum of such bands is, therefore, parabolic in nature with the minimum energy of the parabola at  $E_0$  corresponding to a nonzero angular momentum,  $I_0$ . Figure 8 presents the excitation energy as a function of spin for the DB1 and DB2 bands in this nucleus. Calculations for the DB2 band were carried out assuming a band head with  $E_x = 4.5$  MeV and  $I^\pi = 10^+$ . Also displayed in Fig. 8

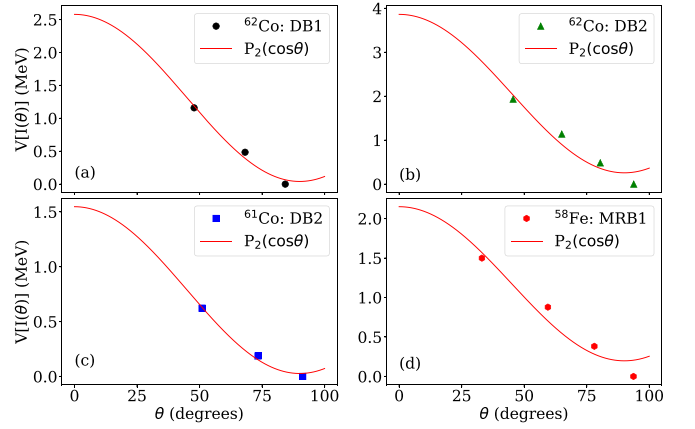


FIG. 9. Effective interaction as a function of the shears angle  $\theta$  for (a) DB1 and (b) DB2 bands in  $^{62}\text{Co}$ . Also shown for comparison are the plots for (c) DB2 band in  $^{61}\text{Co}$  and (d) MRB1 band in  $^{58}\text{Fe}$ . The red curve corresponds to a fit with  $P_2$ -type force dependence.

are some of the observed dipole bands in  $^{61}\text{Co}$  [5] and  $^{58}\text{Fe}$  [39]. The experimental points are seen to follow a strong  $A(I - I_0)^2$  relationship further supporting an interpretation in terms of magnetic rotation for the DB1 and DB2 bands in  $^{62}\text{Co}$ .

Another parameter of interest for magnetic rotation is the shears angle  $\theta$ , e.g., the angle between the proton and neutron spin vectors  $\mathbf{j}_\pi$  and  $\mathbf{j}_\nu$  at the band head. Following the nomenclature of Ref. [40], the shears angle is defined as

$$\cos \theta = \frac{I^2 - j_\pi^2 - j_\nu^2}{2j_\pi j_\nu}, \quad (3)$$

where  $I$  is the total spin. At the band head of a magnetic rotation band,  $\theta = 90^\circ$ . Using  $I = 9$  for the band head of the DB1 band and  $j_\pi = 5$ , Eq. (3) gives  $j_\nu \approx 7$ . Similarly,  $j_\nu \approx 9$  was obtained for the DB2 band. The  $I$ ,  $j_\pi$ , and  $j_\nu$  values can then be used to obtain the value of  $\theta$  as the band progresses to higher angular momentum. Knowing this angle and the level energies, one can also get insight into the effective interaction  $V_{\pi\nu}$  between the proton and the neutron components. The interaction  $V_{\pi\nu}$  defines the change in potential energy caused by the recoupling of the nucleon angular momenta and is given by  $V_{\pi\nu}(I(\theta)) = E(I) - E_{\text{band head}}$  [41]. Figures 9(a) and 9(b) provide the correlation between the  $V(I(\theta))$  parameter, and the shears angle for the DB1 and DB2 bands, respectively, while Figs. 9(c) and 9(d) present the corresponding plots for dipole bands in  $^{61}\text{Co}$  and  $^{58}\text{Fe}$ , respectively. The nature of the effective interaction between protons and neutrons has been discussed in detail in Ref. [43], where it was shown that by taking contributions from spatial forces and symmetry arguments under consideration, the effective interaction can be expanded in terms of even multipoles such that

$$V(\theta) = V_0 + V_2 P_2(\cos \theta) + \dots \quad (4)$$

The energy change along the band ( $E - E_0$ ) is then proportional to  $V_2 P_2(\cos \theta)$  where the sign of  $V_2$  indicates the nature of interaction. The experimental fits in Figs. 9(a)–9(d)

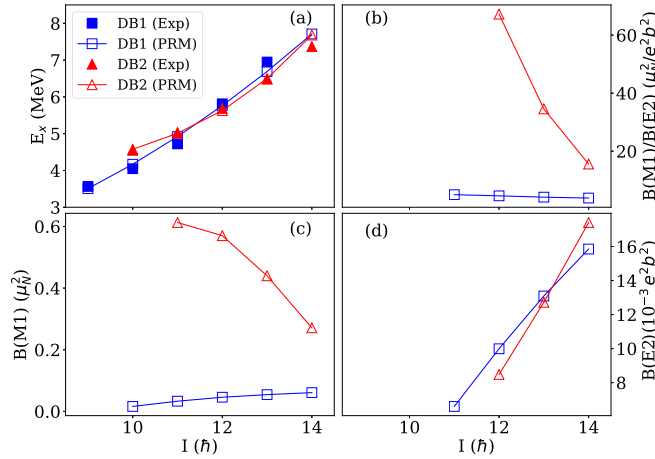


FIG. 10. PRM results in comparison with experimental data for the DB1 and DB2 bands in  $^{62}\text{Co}$ : (a) energy spectra, (b)  $B(M1)/B(E2)$  ratios, (c)  $B(M1)$ , and (d)  $B(E2)$ .

correspond to a  $P_2$ -type dependence with the extracted constant  $V_2 = +1.69$  MeV and  $+2.40$  MeV for the DB1 and the DB2 bands, respectively. The corresponding constants for the dipole bands in  $^{61}\text{Co}$  and  $^{58}\text{Fe}$  have been reported as  $V_2 \approx 1.0$  and  $1.3$  MeV, respectively [5,39].

Based on the striking similarity between the behavior of all these bands, an interpretation of the DB1 and DB2 sequences as magnetic rotation bands appears to be well founded. However, the discussion above is phenomenological and validation through calculations would strengthen the case further. For this purpose, theoretical calculations in the framework of the particle rotor model (PRM) [44–49] were performed. The input configurations and deformation parameters for the PRM were obtained from adiabatic and configuration-fixed constrained covariant density functional theory (CDFT) calculations [50–54] with the point-coupling effective interaction PC-PK1 [55]. The calculated configuration associated with the DB1 band was  $\pi(1f_{7/2})^{-2}(2p_{3/2})^1 \otimes \nu(2p_{3/2})^{-1}$  with a prolate deformation  $\beta = 0.20$ , while that calculated for the DB2 band was  $\pi(1f_{7/2})^{-1} \otimes \nu(1g_{9/2})^2(2p_{3/2})^{-1}$  with  $\beta = 0.28$ . These two configurations are the lowest two excited positive-parity particle-hole configurations (with excitation energies 1.63 MeV and 5.38 MeV, respectively) with respect to the ground state in the CDFT calculations. Another possibility for an excited positive-parity configuration is  $\pi(1g_{9/2})^1 \otimes \nu(1g_{9/2})^1$  at an excitation energy of 7.33 MeV and a deformation of  $\beta = 0.33$ . However, this particle-particle configuration leads to a  $\Delta I = 2$  band and is, thus, inconsistent with the experimental data. Of note within the chosen configuration for the DB1 band is the absence of a high- $j$  valence particle that would be responsible for the formation of a shear. Nevertheless, the calculated energy spectra as a function of spin compare well with the experimental data [see Fig. 10(a)], where calculated moments of inertia  $\mathcal{J}_0 = 7.875$  and  $3.0 \hbar^2/\text{MeV}$  were adopted for the DB1 and DB2 bands, respectively. Note that for each configuration, the band head energy as predicted by PRM was normalized to its respective experimental value.

The PRM was utilized further to obtain electromagnetic transition probabilities and to examine their trend as a function of angular momentum. Typical characteristics of magnetic rotation bands are strongly enhanced  $M1$  transitions at low spins as well as a decreasing trend in  $M1$  strength with increasing angular momentum. In contrast, the associated  $E2$  transitions of the bands are very weak. Figs. 10(b)–10(d) display the calculated  $B(M1)/B(E2)$  ratios,  $B(M1)$ , and  $B(E2)$  strengths as a function of spin for the DB1 and DB2 bands. As expected, the computed  $B(E2)$  values for the bands are small ( $<0.02 e^2b^2$ ) and increase with spin [Fig. 10(d)]. However, the anticipated, characteristic large  $M1$  strength and its decrease with spin is calculated to occur only for the DB2 sequence. The corresponding strength is small and almost constant in the DB1 case [Fig. 10(c)]. As a result, the computed  $B(E2)/B(M1)$  ratios as a function of spin exhibit a strikingly different pattern as well. The differences between the two calculated bands can be traced to the absence of a high- $j$  particle in the DB1 configuration discussed above. A theoretical study detailing further the PRM calculations is, however, beyond the scope of the present work and will be published elsewhere [56].

## V. CONCLUSIONS

A detailed study of the odd-odd  $^{62}\text{Co}$  nucleus was performed following a multinucleon transfer reaction. A considerable extension to the level scheme was achieved with levels up to  $I^\pi = (13^+)$  at an excitation energy of 6.9 MeV. Firm spin and parity assignments were possible based on angular distribution measurements. Various single-particle level structures were observed at low spins and large-scale spherical shell-model calculations were employed to investigate the underlying structure. However, the shell model was found to reproduce the experiment rather poorly and the exclusion of the  $g_{9/2}$  orbital within the model space is likely responsible for the observed discrepancy. The development of a larger model space including the  $g_{9/2}$  orbital is, hence, imperative for the study of neutron-rich nuclei within the  $A \approx 60$  region. Such studies, while beyond the scope of the present work, are becoming practical (see for example, Ref. [57]). In addition to these single-particle structures, two dipole bands (DB1 and DB2) were also observed at moderate spins. A phenomenological study of the two bands suggests a possible magnetic rotation character. However, a higher statistics experiment would be helpful as it could potentially extend the bands to higher spins and enable the extraction of transition probabilities. Such data would also test further the PRM calculations presented above, which were thus far shown to be consistent with the magnetic rotation picture only for band DB2.

## ACKNOWLEDGMENTS

The authors acknowledge Prof. C. J. Lister for helpful discussions that were instrumental in shaping the introduction of the present work. This work was supported in part by the U.S. Department of Energy, Office of Science, Office of Nuclear Physics, under Contract No. DE-AC02-06CH11357 and Grants No. DE-FG02-94ER40834, No.



DE-FG02-08ER41556, No. DE-FG02-94ER40848, and No. DE-SC0020451, by the NSF under Contract No. PHY-0606007, and by the UNC Startup Funds of ADA. This

research used resources of Argonne National Laboratory's ATLAS facility, which is a DOE Office of Science User Facility.

- [1] M. Bernas, P. Dessagne, M. Langevin, J. Payet, F. Pougheon, and P. Roussel, *Phys. Lett. B* **113**, 279 (1982).
- [2] S. Zhu, R. V. F. Janssens, M. P. Carpenter, C. J. Chiara, R. Broda, B. Fornal, N. Hoteling, W. Królas, T. Lauritsen, T. Pawlat, D. Seweryniak, I. Stefanescu, J. R. Stone, W. B. Walters, X. Wang, and J. Wrzesiński, *Phys. Rev. C* **85**, 034336 (2012).
- [3] M. Albers, S. Zhu, A. D. Ayangeakaa, R. V. F. Janssens, J. Gellanki, I. Ragnarsson, M. Alcorta, T. Baugher, P. F. Bertone, M. P. Carpenter, C. J. Chiara, P. Chowdhury, H. M. David, A. N. Deacon, B. DiGiovine, A. Gade, C. R. Hoffman, F. G. Kondev, T. Lauritsen, C. J. Lister *et al.*, *Phys. Rev. C* **94**, 034301 (2016).
- [4] M. Albers, S. Zhu, R. V. F. Janssens, J. Gellanki, I. Ragnarsson, M. Alcorta, T. Baugher, P. F. Bertone, M. P. Carpenter, C. J. Chiara, P. Chowdhury, A. N. Deacon, A. Gade, B. DiGiovine, C. R. Hoffman, F. G. Kondev, T. Lauritsen, C. J. Lister, E. A. McCutchan, D. S. Moerland *et al.*, *Phys. Rev. C* **88**, 054314 (2013).
- [5] A. D. Ayangeakaa, S. Zhu, R. V. F. Janssens, M. P. Carpenter, M. Albers, M. Alcorta, T. Baugher, P. F. Bertone, C. J. Chiara, P. Chowdhury, H. M. David, A. N. Deacon, B. DiGiovine, A. Gade, C. R. Hoffman, F. G. Kondev, T. Lauritsen, C. J. Lister, E. A. McCutchan, D. S. Moerland *et al.*, *Phys. Rev. C* **91**, 044327 (2015).
- [6] D. W. Luo, C. Xu, Y. K. Wang, Z. H. Li, R. A. Bark, S. Q. Zhang, H. Hua, S. Y. Wang, J. Peng, X. Q. Li, H. Y. Wu, X. Wang, C. G. Wu, Q. T. Li, J. Lin, Y. Jin, W. Z. Xu, L. Mu, J. Meng, F. R. Xu *et al.*, *Phys. Rev. C* **105**, 024305 (2022).
- [7] R. Broda, B. Fornal, W. Królas, T. Pawlat, D. Bazzacco, S. Lunardi, C. Rossi-Alvarez, R. Menegazzo, G. de Angelis, P. Bednarczyk, J. Rico, D. De Acuña, P. J. Daly, R. H. Mayer, M. Sferrazza, H. Grawe, K. H. Maier, and R. Schubart, *Phys. Rev. Lett.* **74**, 868 (1995).
- [8] J. Prisciandaro, P. Mantica, B. Brown, D. Anthony, M. Cooper, A. Garcia, D. Groh, A. Komives, W. Kumarasiri, P. Lofy, A. Oros-Peusquens, S. Tabor, and M. Wiedeking, *Phys. Lett. B* **510**, 17 (2001).
- [9] E. Leistenschneider, M. P. Reiter, S. Ayet San Andrés, B. Kootte, J. D. Holt, P. Navrátil, C. Babcock, C. Barbieri, B. R. Barquest, J. Bergmann, J. Bollig, T. Brunner, E. Dunling, A. Finlay, H. Geissel, L. Graham, F. Greiner, H. Hergert, C. Hornung, C. Jesch *et al.*, *Phys. Rev. Lett.* **120**, 062503 (2018).
- [10] A. Huck, G. Klotz, A. Knipper, C. Miehe, C. Richard-Serre, G. Walter, A. Poves, H. L. Ravn, and G. Marguier, *Phys. Rev. C* **31**, 2226 (1985).
- [11] A. Gade, R. V. F. Janssens, D. Bazin, R. Broda, B. A. Brown, C. M. Campbell, M. P. Carpenter, J. M. Cook, A. N. Deacon, D.-C. Dinca, B. Fornal, S. J. Freeman, T. Glasmacher, P. G. Hansen, B. P. Kay, P. F. Mantica, W. F. Mueller, J. R. Terry, J. A. Tostevin, and S. Zhu, *Phys. Rev. C* **74**, 021302(R) (2006).
- [12] R. V. F. Janssens, B. Fornal, P. F. Mantica, B. A. Brown, R. Broda, P. Bhattacharyya, M. P. Carpenter, M. Cinausero, P. J. Daly, A. D. Davies, T. Glasmacher, Z. W. Grabowski, D. E. Groh, M. Honma, F. G. Kondev, W. Królas, T. Lauritsen, S. N. Liddick, S. Lunardi, N. Marginean *et al.*, *Phys. Lett. B* **546**, 55 (2002).
- [13] M. L. Cortés, W. Rodriguez, P. Doornenbal, A. Obertelli, J. D. Holt, J. Menéndez, K. Ogata, A. Schwenk, N. Shimizu, J. Simonis, Y. Utsuno, K. Yoshida, L. Achouri, H. Baba, F. Browne, D. Calvet, F. Château, S. Chen, N. Chiga, A. Corsi *et al.*, *Phys. Rev. C* **102**, 064320 (2020).
- [14] D. Steppenbeck, S. Takeuchi, N. Aoi, P. Doornenbal, M. Matsushita, H. Wang, H. Baba, N. Fukuda, S. Go, M. Honma, J. Lee, K. Matsui, S. Michimasa, T. Motobayashi, D. Nishimura, T. Otsuka, H. Sakurai, Y. Shiga, P.-A. Söderström, T. Sumikama *et al.*, *Nature (London)* **502**, 207 (2013).
- [15] D.-C. Dinca, R. V. F. Janssens, A. Gade, D. Bazin, R. Broda, B. A. Brown, C. M. Campbell, M. P. Carpenter, P. Chowdhury, J. M. Cook, A. N. Deacon, B. Fornal, S. J. Freeman, T. Glasmacher, M. Honma, F. G. Kondev, J.-L. Lecouey, S. N. Liddick, P. F. Mantica, W. F. Mueller *et al.*, *Phys. Rev. C* **71**, 041302(R) (2005).
- [16] S. Chen, J. Lee, P. Doornenbal, A. Obertelli, C. Barbieri, Y. Chazono, P. Navrátil, K. Ogata, T. Otsuka, F. Raimondi, V. Somà, Y. Utsuno, K. Yoshida, H. Baba, F. Browne, D. Calvet, F. Château, N. Chiga, A. Corsi, M. L. Cortés *et al.*, *Phys. Rev. Lett.* **123**, 142501 (2019).
- [17] H. N. Liu, A. Obertelli, P. Doornenbal, C. A. Bertulani, G. Hagen, J. D. Holt, G. R. Jansen, T. D. Morris, A. Schwenk, R. Stroberg, N. Achouri, H. Baba, F. Browne, D. Calvet, F. Château, S. Chen, N. Chiga, A. Corsi, M. L. Cortés, A. Delbart *et al.*, *Phys. Rev. Lett.* **122**, 072502 (2019).
- [18] R. Broda, T. Pawlat, W. Królas, R. V. F. Janssens, S. Zhu, W. B. Walters, B. Fornal, C. J. Chiara, M. P. Carpenter, N. Hoteling, L. W. Iskra, F. G. Kondev, T. Lauritsen, D. Seweryniak, I. Stefanescu, X. Wang, and J. Wrzesiński, *Phys. Rev. C* **86**, 064312 (2012).
- [19] I. Bala, S. C. Pancholi, M. K. Raju, A. Dhal, S. Saha, J. Sethi, T. Trivedi, R. Raut, S. S. Ghugre, R. Palit, R. P. Singh, and S. Muralithar, *Phys. Rev. C* **104**, 044302 (2021).
- [20] S. Zhu, A. N. Deacon, S. J. Freeman, R. V. F. Janssens, B. Fornal, M. Honma, F. R. Xu, R. Broda, I. R. Calderin, M. P. Carpenter, P. Chowdhury, F. G. Kondev, W. Królas, T. Lauritsen, S. N. Liddick, C. J. Lister, P. F. Mantica, T. Pawlat, D. Seweryniak, J. F. Smith *et al.*, *Phys. Rev. C* **74**, 064315 (2006).
- [21] N. Hoteling, C. J. Chiara, R. Broda, W. B. Walters, R. V. F. Janssens, M. Hjorth-Jensen, M. P. Carpenter, B. Fornal, A. A. Hecht, W. Królas, T. Lauritsen, T. Pawlat, D. Seweryniak, X. Wang, A. Wöhr, J. Wrzesiński, and S. Zhu, *Phys. Rev. C* **82**, 044305 (2010).
- [22] A. N. Deacon, S. J. Freeman, R. V. F. Janssens, M. Honma, M. P. Carpenter, P. Chowdhury, T. Lauritsen, C. J. Lister, D. Seweryniak, J. F. Smith, S. L. Tabor, B. J. Varley, F. R. Xu, and S. Zhu, *Phys. Rev. C* **76**, 054303 (2007).
- [23] O. Sorlin, S. Leenhardt, C. Donzaud, J. Duprat, F. Azaiez, F. Nowacki, H. Grawe, Z. Dombrádi, F. Amorini, A. Astier, D. Baiborodin, M. Bellegruic, C. Borcea, C. Bourgeois, D. M. Cullen, Z. Dlouhy, E. Dragulescu, M. Górska, S. Grévy, D. Guillemaud-Mueller *et al.*, *Phys. Rev. Lett.* **88**, 092501 (2002).

- [24] M. Stryjczyk, Y. Tsunoda, I. G. Darby, H. De Witte, J. Diriken, D. V. Fedorov, V. N. Fedosseev, L. M. Fraile, M. Huyse, U. Köster, B. A. Marsh, T. Otsuka, D. Pauwels, L. Popescu, D. Radulov, M. D. Seliverstov, A. M. Sjödin, P. Van den Bergh, P. Van Duppen, M. Venhart *et al.*, *Phys. Rev. C* **98**, 064326 (2018).
- [25] D. G. Gardner and W. W. Meinke, *Phys. Rev.* **107**, 1628 (1957).
- [26] I. Preiss and R. Fink, *Nucl. Phys.* **15**, 326 (1960).
- [27] D. Bachner, H. Kelleter, B. Schmidt, and W. Seliger, *Nucl. Phys. A* **184**, 609 (1972).
- [28] E. K. Warburton, J. W. Olness, A. M. Nathan, and A. R. Poletti, *Phys. Rev. C* **18**, 1637 (1978).
- [29] F. Recchia, S. M. Lenzi, S. Lunardi, E. Farnea, A. Gadea, N. Märginean, D. R. Napoli, F. Nowacki, A. Poves, J. J. Valiente-Dobón, M. Axiotis, S. Aydin, D. Bazzacco, G. Benzoni, P. G. Bizzeti, A. M. Bizzeti-Sona, A. Bracco, D. Bucurescu, E. Caurier, L. Corradi *et al.*, *Phys. Rev. C* **85**, 064305 (2012).
- [30] M. Honma, T. Otsuka, B. A. Brown, and T. Mizusaki, *Eur. Phys. J. A* **25**, 499 (2005).
- [31] I.-Y. Lee, *Nucl. Phys. A* **520**, c641 (1990).
- [32] D. Radford, *Nucl. Instrum. Methods Phys. Res. A* **361**, 297 (1995).
- [33] K. B. Howard, Structure Effects on the Giant Monopole Resonance and Determinations of the Nuclear Incompressibility, Ph.D. thesis, University of Notre Dame, 2020.
- [34] N. Sensharma, Wobbling Motion in Nuclei: Transverse, Longitudinal and Chiral, Ph.D. thesis, University of Notre Dame, 2021.
- [35] A. Krämer-Flecken, T. Morek, R. Lieder, W. Gast, G. Hebbinghaus, H. Jäger, and W. Urban, *Nucl. Instrum. Methods Phys. Res. A* **275**, 333 (1989).
- [36] A. L. Nichols, B. Singh, and J. K. Tuli, *Nucl. Data Sheets* **113**, 973 (2012).
- [37] B. Brown and W. Rae, *Nucl. Data Sheets* **120**, 115 (2014).
- [38] M. Hjorth-Jensen, T. T. S. Kuo, and E. Osnes, *Phys. Rep.* **261**, 125 (1995).
- [39] D. Steppenbeck, R. V. F. Janssens, S. J. Freeman, M. P. Carpenter, P. Chowdhury, A. N. Deacon, M. Honma, H. Jin, T. Lauritsen, C. J. Lister, J. Meng, J. Peng, D. Seweryniak, J. F. Smith, Y. Sun, S. L. Tabor, B. J. Varley, Y.-C. Yang, S. Q. Zhang, P. W. Zhao *et al.*, *Phys. Rev. C* **85**, 044316 (2012).
- [40] A. O. Macchiavelli, R. M. Clark, P. Fallon, M. A. Deleplanque, R. M. Diamond, R. Krücken, I. Y. Lee, F. S. Stephens, S. Asztalos, and K. Vetter, *Phys. Rev. C* **57**, R1073 (1998).
- [41] A. O. Macchiavelli, R. M. Clark, M. A. Deleplanque, R. M. Diamond, P. Fallon, I. Y. Lee, F. S. Stephens, and K. Vetter, *Phys. Rev. C* **58**, R621 (1998).
- [42] S. Frauendorf, *Nucl. Phys. A* **557**, 259c (1993).
- [43] R. M. Clark and A. O. Macchiavelli, *Annu. Rev. Nucl. Part. Sci.* **50**, 1 (2000).
- [44] Q. B. Chen, B. F. Lv, C. M. Petrache, and J. Meng, *Phys. Lett. B* **782**, 744 (2018).
- [45] E. Streck, Q. B. Chen, N. Kaiser, and Ulf-G. Meißner, *Phys. Rev. C* **98**, 044314 (2018).
- [46] J. Peng and Q. B. Chen, *Phys. Lett. B* **793**, 303 (2019).
- [47] Q. B. Chen, S. Frauendorf, and C. M. Petrache, *Phys. Rev. C* **100**, 061301(R) (2019).
- [48] Q. B. Chen, S. Frauendorf, N. Kaiser, U.-G. Meißner, and J. Meng, *Phys. Lett. B* **807**, 135596 (2020).
- [49] J. Peng and Q. B. Chen, *Phys. Lett. B* **806**, 135489 (2020).
- [50] J. Meng, J. Peng, S. Q. Zhang, and S.-G. Zhou, *Phys. Rev. C* **73**, 037303 (2006).
- [51] J. Meng, H. Toki, S. Zhou, S. Zhang, W. Long, and L. Geng, *Prog. Part. Nucl. Phys.* **57**, 470 (2006).
- [52] J. Meng, J. Y. Guo, Z. P. Li, H. Z. Liang, W. H. Long, Y. F. Niu, Z. M. Niu, J. M. Yao, Y. Zhang, P. W. Zhao, and S. G. Zhou, *Prog. Phys.* **31**, 199 (2011).
- [53] J. Meng, *Relativistic Density Functional for Nuclear Structure* (World Scientific, Singapore, 2016).
- [54] J. Peng and Q. B. Chen, *Phys. Rev. C* **98**, 024320 (2018).
- [55] P. W. Zhao, Z. P. Li, J. M. Yao, and J. Meng, *Phys. Rev. C* **82**, 054319 (2010).
- [56] Q. B. Chen (to be published).
- [57] A. Gade, R. V. F. Janssens, D. Bazin, P. Farris, A. M. Hill, S. M. Lenzi, J. Li, D. Little, B. Longfellow, F. Nowacki, A. Poves, D. Rhodes, J. A. Tostevin, and D. Weisshaar, *Phys. Rev. C* **103**, 014314 (2021).